Chinese Chemical Letters 34 (2023) 107811

Contents lists available at ScienceDirect

Chinese Chemical Letters

journal homepage: www.elsevier.com/locate/cclet

Bidirectionally polarizing surface chemistry of heteroatom-doped carbon matrix towards fast and longevous lithium-sulfur batteries

Hongyang Li[a], Bo Cai[b], Yingze Song[c], Wenlong Cai[d,*], Gaoran Li[a,*]

[a] MIIT Key Laboratory of Advanced Display Materials and Devices, College of Materials Science and Engineering, Nanjing University of Science and Technology, Nanjing 210094, China
[b] State Key Laboratory of Organic Electronics and Information Displays & Institute of Advanced Materials (IAM), Nanjing University of Posts & Telecommunications, Nanjing 210023, China
[c] State Key Laboratory of Environmental-Friendly Energy Materials, School of Materials Science and Engineering, Southwest University of Science and Technology, Mianyang 621010, China
[d] Department of Advanced Energy Materials, College of Materials Science and Engineering, Sichuan University, Chengdu 610064, China

ARTICLE INFO

Article history:
Received 5 July 2022
Revised 23 July 2022
Accepted 6 September 2022
Available online 29 September 2022

Keywords:
Lithium-sulfur battery
Facile synthesis
Heteroatom doping
Bidirectional polarization
Shuttle effect

ABSTRACT

Herein, a bidirectional polarization strategy is proposed for hosting efficient and durable lithium-sulfur battery (Li-S) electrochemistry. By co-doping electronegative N and electropositive B in graphene matrix (BNrGO), the bidirectional electron redistribution enables a higher polysulfide affinity over its mono-doped counterparts, contributing to strong sulfur immobilization and fast conversion kinetics. As a result, BNrGO as the cathode host matrix realizes excellent cycling stability over 1000 cycles with a minimum capacity fading of 0.027% per cycle, and superb rate capability up to 10 C. Meanwhile, decent areal capacity (6.46 mAh/cm^2) and cyclability (300 cycles) are also achievable under high sulfur loading and limited electrolyte. This work provides instructive insights into the interaction between doping engineering and sulfur electrochemistry for pursuing superior Li-S batteries.

© 2023 Published by Elsevier B.V. on behalf of Chinese Chemical Society and Institute of Materia Medica, Chinese Academy of Medical Sciences.

Lithium-sulfur (Li-S) batteries present one of the most promising solutions to efficient and affordable energy storage. The room-temperature sulfur electrochemistry delivers attractive merits of high capacity (1675 mAh/g), abundant reserves, wide geographical distribution, and environmental benignity [1,2]. However, these benefits are accompanied by several critical challenges. One notorious of them is the so-called "shuttle effect", which is aroused by the high solubility and mobility of the intermediate lithium polysulfide (LPS) in the electrolyte [3–5]. Combined with the insulating nature of sulfur and its large volume variation upon lithiation/delithiation, sulfur electrochemistry encounters serious active material loss, electrode passivation, and coulombic inefficiency, struggling with unsatisfactory cycling and rate capabilities to meet the practical demands [6–8].

Given these issues, carbon-based host matrix is a promising strategy to improve redox reversibility due to its lightweight, excellent conductivity, and good structural customizability [9]. During the past few years, numerous carbon nanostructures have been explored including nanospheres, nanotubes, nanosheets, aerogel, *etc*., which provide critical conductivity support and well-designed architecture that physically confines the sulfur species against their shuttling behaviors [10–12]. Despite certain advances, the mere physical effects were found hard to sufficiently confine LPS. This is determined by the non-polar nature of the carbon surface with intrinsically limited chemical affinity to the weak-polar LPS [13–15]. Hence, surface engineering towards higher polarity and stronger LPS affinity is desired to combine physical and chemical immobilizations, yet the rational design is also necessary to avoid excessive compromise in conduction properties.

Given this, heteroatomic doping, which gingerly alters the surface chemistry with a well-maintained carbon lattice, presents a modest but reliable strategy to balance the chemical polarity and electrical conductivity. Recently, heteroatom-doped carbons have been actively studied, including mono-, dual, and multi-doped configurations, with varying degrees of impact on Li-S battery performance [16–18]. However, studies on the synergy among the heteroatoms, the underlying mechanism, as well as the impact on sulfur electrochemistry are still limited. Essentially, the rationale behind the doping strategy lies in the electron redistribution in carbon lattice. Thus, the collaboration among elements with a large difference in electron-donating/accepting abilities could establish higher heterogeneity of local electron density with higher chemical polarity, which potentially accesses stronger host-guest inter-

* Corresponding authors.
E-mail addresses: caiwl@scu.edu.cn (W. Cai), gaoranli@njust.edu.cn (G. Li).

https://doi.org/10.1016/j.cclet.2022.107811
1001-8417/© 2023 Published by Elsevier B.V. on behalf of Chinese Chemical Society and Institute of Materia Medica, Chinese Academy of Medical Sciences.

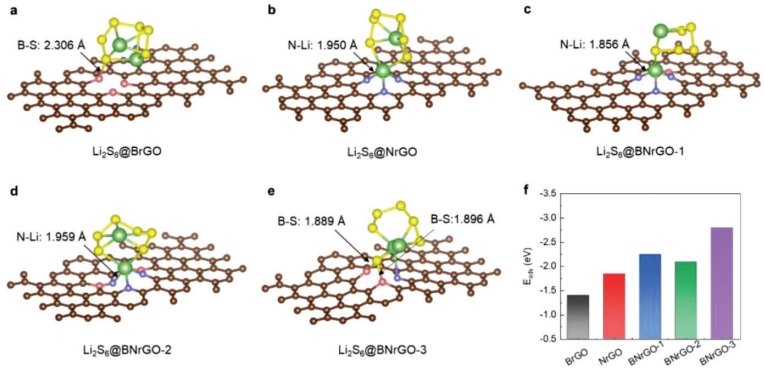

Fig. 1. (a-e) Geometrically stable configurations and (f) adsorption energies of Li_2S_6 on different matrix surfaces.

action towards superior sulfur electrochemistry. In addition, conventional synthesis of heteroatom-doped carbons, particularly for those co- and multi-doped, is generally complex and costly, involving ionic liquid precursor, multi-step procedures, high-temperature treatment, *etc*., which hardly suits the large-scale fabrication and commercialization [19–21]. Therefore, well-designed surface chemical engineering with facile and cost-effective feasibility is desired for high-performance and practically viable Li-S batteries.

In this contribution, we proposed a bidirectional polarization strategy and intentionally designed a B, N co-doped reduced graphene oxide (BNrGO), as a case study, for hosting durable sulfur electrochemistry. BNrGO was prepared by reducing graphene oxide (GO) with ammonia borane (AB), which is facile, fast and cost-effective. In the BNrGO structure, nitrogen with higher electronegativity over carbon draws electrons and forms the electron-rich domains, while boron with lower electronegativity serves oppositely as the electron-doner to form the electron-lean domains. As such, the synergistic co-doping renders charge redistribution in the sp^2 carbon plane, and bidirectionally polarizes the surface chemistry with stronger chemical affinity to LPS. As a result, the dual-adsorption mechanism was established that outperforms its counterparts with mere N or B doping (NrGO or BrGO), enabling encouraging electrochemical improvements with excellent cycling stability (1000 cycles) and rate capability (10 C), as well as decent performances under high sulfur loading (6.6 mg/cm^2) and low electrolyte-to-sulfur ratio (E/S, 5.5 mL/g).

Firstly, density functional theory (DFT) calculation was carried out based on simplified graphene models (Fig. S1 in Supporting information) to predict the charge redistributions. Three co-doping patterns were simulated, *i.e*., *ortho*-, *meta* and *para*-coupling of B and N, which were denoted as *o*-BNrGO, *m*-BNrGO and *p*-BNrGO, respectively. Fig. S2 (Supporting information) shows the charge distributions of different configurations, where the blue and red circles highlight respectively the B and N sites. It is noticed that B doping contributes to the electron-deficient region due to the less electron and lower electronegativity of B compared with C. On the contrary, N-doping renders the electron-rich region as N has a higher electron-withdrawing ability over C. Such tendency can be also found in all the co-doped structures. In addition, the corresponding charge difference density patterns are depicted in Fig. S3 (Supporting information), with the calculated Bader charge summarized in Table S1 (Supporting information). The B atom in BrGO delivers a Bader charge of −1.884 e due to its electron-donating character, while the high electronegativity of N strongly accepts electrons from the adjacent carbon, resulting in a Bader charge of 1.160 e in NrGO. This trend of electron transfer is inherited in all the co-doped scenarios and is notably intensified to varying extents in different configurations. Based on this, it can be comprehended that the combination of B and N doping readily establishes a more undulating electrostatic potential distribution, rendering a higher polar surface with enriched active sites for host-guest interactions.

Given this, the interaction behaviors between LPS and host matrix were further simulated. The same lattice deficiency that knocks off one sp^2 carbon atom was applied with different edge-type heteroatoms to alleviate potential steric hindrance. Fig. 1 shows the geometrically stable configurations of Li_2S_6 adsorption on different surfaces. It is noted that the electron-deficient B site tends to bond with the negatively-charged S in polysulfide, while the electron-rich N site attracts Li to form the N-Li-S bridging bond similar to that described as the "lithium bond" [22,23]. This well conforms to the Lewis acid-base interaction patterns and suggests the dual-adsorptive activity of B and N sites for host-guest interaction. More importantly, the co-doped matrixes exhibit much higher adsorbability likely due to the intensified heterogeneity of charge distribution and the enhanced chemical polarity compared with the mono-doped ones. Three typical adsorption configurations for BNrGO were demonstrated. When codoped with an adjacent B, BNrGO-1 (Fig. 1c) enables a much-shortened N-Li bond (1.856 Å) compared with that of NrGO (1.950 Å) at the same spot (Fig. 1b). Meanwhile, BNrGO-3 (Fig. 1e) reveals much shorter B-S bonds (1.889 and 1.896 Å) than that on the BrGO surface (2.306 Å, Fig. 1a). Thus, the co-doping reinforces Li-N and B-S coordinations attributed to the enhanced polarity, contributing to stronger chemical affinities to LPS with higher adsorption energies up to −2.79 eV (BNrGO-3) compared with the mono-doped counterparts (−1.403 and −1.845 eV for BrGO and NrGO, respectively, Fig. 1f). These results strongly confirm the great potential of the bidirectional polarization strategy for confining LPS towards durable sulfur electrochemistry.

Based on the computational prediction, the experimental verification was implemented by synthesizing BNrGO *via* a facile, one-pot, and solution-based method (Fig. S4 in Supporting information). Ammonia borane (AB) was specifically employed as the simultaneous reductant and dopant. For comparison, NrGO and BrGO were also prepared under similar conditions. As shown in Figs. 2a and b, the as-prepared BNrGO exhibits a thin and wrinkled 2D structure inheriting from the parent GO. The nanosheets stagger and interweave into a long-extending network, which provides an excellent long-range conductivity for electrochemical reactions. The TEM image confirms the 2D structure with a large planar size up to several micrometers (Fig. 2c). Moreover, the EDS element mapping (Fig. 2d) verifies the co-existence and uniform distributions of N and B in BNrGO. Similar morphological structures are also obtained for BrGO and NrGO as shown in Fig. S5 (Supporting information). Apart from that, the porous texture was studied by N_2 adsorption-desorption. Fig. S6a (Supporting information) shows a type IV isotherm with an H2 hysteresis loop, suggesting the hi-

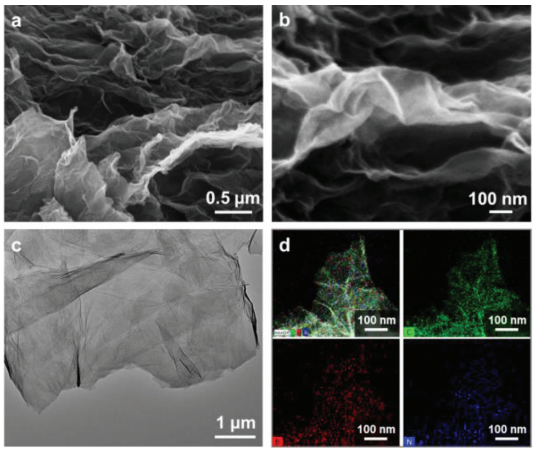

Fig. 2. (a, b) SEM images, (c) TEM image, and (d) EDS element mapping of BNrGO.

erarchical porosity with rich mesopores in BNrGO, which can be also confirmed by the pore size distribution (Fig. S6b in Supporting information). As a result, a decently high specific surface area of *ca.* 293.0 m^2/g is determined for BNrGO, which affords large space for sulfur accommodation, abundant channels for ion/mass transfer, and massive active interfaces for host-guest interactions.

The XRD pattern in Fig. S7 (Supporting information) shows a sharp and typical peak at 11.76° for the parent GO. After the wet conversion, this peak shifts to around 24.15° with a narrowed interlayer spacing, signifying the successful reduction into rGO [24]. Moreover, Raman spectra were collected to further study the carbon lattice structure. As shown in Fig. S8 (Supporting information), GO shows strong peaks at Raman shift of around 1340 and 1580 cm^{-1}, which refer to the D band and G band respectively of the carbon lattice. The D band reflects the breathing vibration mode of the hybridized carbon rings, while the G band is ascribed to the stretching vibration mode of the sp^2 carbon pairs [25,26]. The intensity ratio of D to G bands (I_D/I_G) is a general indicator of the defect level of carbon lattice. It can be noticed that BrGO, NrGO, and BNrGO deliver much higher I_D/I_G than that of the parent GO, confirming the abundant heteroatom doping within the obtained 2D carbon lattices.

Given this, the surface chemistry was probed by X-ray photoelectron spectroscopy (XPS). The survey spectrum confirms the coexistence of B and N in BNrGO (Fig. S9 in Supporting information), as well as the individual presence of B and N in BrGO and NrGO, respectively (Figs. S10a and c). The high-resolution C 1s spectrum in Fig. 3a delivers three subpeaks at 284.8, 286.2 and 288.5 eV referring to the C-C, C-N/O and O-C=O species, respectively, suggesting the N doping and the partial surface oxidization of BNrGO [27]. The deconvolution of the N 1s spectrum witnesses five sub-peaks, which are assigned to the N-B, pyridinic N, pyrrolic N, graphitic N and NO_x species (Fig. 3b) [28]. The emergence of the N-B peak evidences the successful co-doping of B and N, as well as the strong interaction between them. Consistently, the B-N/O and B-C peaks are detected in the B 1s spectrum (Fig. 3c), confirming the B doping in the matrix [29,30]. Similar doping signals can be also found for BrGO and NrGO (Figs. S10b and d in Supporting information), but without the B-N conjunction due to the single doping. The XPS analysis reflects a B content of 2.24% in BrGO, N content of 4.47% in NrGO, and the respective B and N content of 1.76% and 2.75% in BNrGO.

These doping structures are expected to impose polar surface and desirable polysulfide adsorption, as also predicted above. For proof of concept, the static adsorption test was carried out by immersing the same amount of different samples in 3 mmol/L Li_2S_6 solutions. The multi-layered graphene (MLG) obtained by annealing GO at a high temperature of 2000 °C was applied as a control sample with minimum heteroatom doping [31,32]. As shown in Fig. 3d, the blank Li_2S_6 solution remains the typical orange color after resting for 12 h, while MLG renders a slightly lighter color due to certain physical adsorption. By comparison, the doped samples enable more significant decoloration, while BNrGO contributes to an almost colorless solution. Such intuitional contrast can be more quantificationally understood by the UV–vis test, where BNrGO delivers the lowest absorbance intensity among all the samples, signifying the least polysulfide residue in the supernatant and its highest capability of adsorbing polysulfides. The underlying adsorption mechanism was further studied by XPS analysis. Fig. 3e shows the S 2p spectra of Li_2S_6, as an LPS representative, before and after adsorption by BNrGO. Typically, Li_2S_6 shows two pairs of peaks assigned respectively to the terminal (S_T) and bridging (S_B) sulfur species [33,34]. Notably, these peaks shift to higher binding energy (BE) after adsorption by BNrGO. This is ascribed to the electron transfer from the Lewis-base polysulfide anions to the Lewis-acid B site in BNrGO upon the interaction. The thiosulfate and polythionate species are also detected after adsorption, which is likely due to the partial oxidization of polysulfide. Besides, the emergence of a new peak assigned to the Li-N bonding can be witnessed in the Li 1s spectra (Fig. 3f), manifesting the formation of the "lithium bond"-like configuration upon the adsorption [22,35]. These results well echo the DFT calculations and confirm the strong chemical interactions between LPS and BNrGO, which would effectively adsorb the active species for shuttle inhibition and reaction promotion.

To validate these potential improvements, Li-S coin cells were assembled for electrochemical evaluations. The sulfur-based composite with a sulfur loading of *ca.* 71.4 wt% (Fig. S11 in Supporting information) was prepared *via* the conventional melt-diffusion method, while the uniform sulfur impregnation was confirmed by SEM observation (Fig. S12 in Supporting information). Fig. 4a shows the CV profiles of the Li-S cells based on different cathode host materials. Two pairs of redox peaks can be noticed, corresponding to the conversions between element sulfur and high-order polysulfide (peak C1 and A1), and that between low-order polysulfide and insoluble Li_2S/Li_2S_2 (peak C2 and A2), respectively [36]. It is worth noting that the BNrGO cell exhibits the highest peak intensity, sharpest peak shape, and lowest redox polarization, indicating its most facile and efficient sulfur reaction. To further study the kinetic behavior, the Tafel plots for the peak pair (C2 and A2), which is regarded as a more kinetically-limiting process, are compared in Fig. S13 (Supporting information). The BNrGO cell exhibits the lowest Tafel slopes at both the cathodic and anodic processes, illustrating its lowest energy barrier for the solid-liquid conversions. Consistently, the galvanostatic charge-discharge curves show two discharge plateaus due to the multi-step sulfur reduction (Fig. 4b). It is noted that the BNrGO cell undergoes the least voltage hysteresis with the smallest potential gap between the charge and discharge curves, along with the highest ratio of low-plateau to high-plateau capacities (Q_L/Q_H, Fig. S14 in Supporting information), which is an important indicator of reaction efficiency [37]. Such improvement can be also verified by symmetric cells as shown in Fig. S15 (Supporting information), where the CV curve of the BNrGO cell exhibits the highest current response and smallest redox potential gap, manifesting much faster LPS conversions compared with the BrGO and NrGO counterparts. These comparisons strongly illustrate the best reaction kinetics enabled by BNrGO, which establishes a bidirectionally polarized surface chemistry with enhanced sulfur affinity and facilitates the electrochemical conversions thereon.

Furthermore, a much higher initial capacity of 1352.7 mAh/g can be obtained by the BNrGO cell at C/5 compared with BrGO

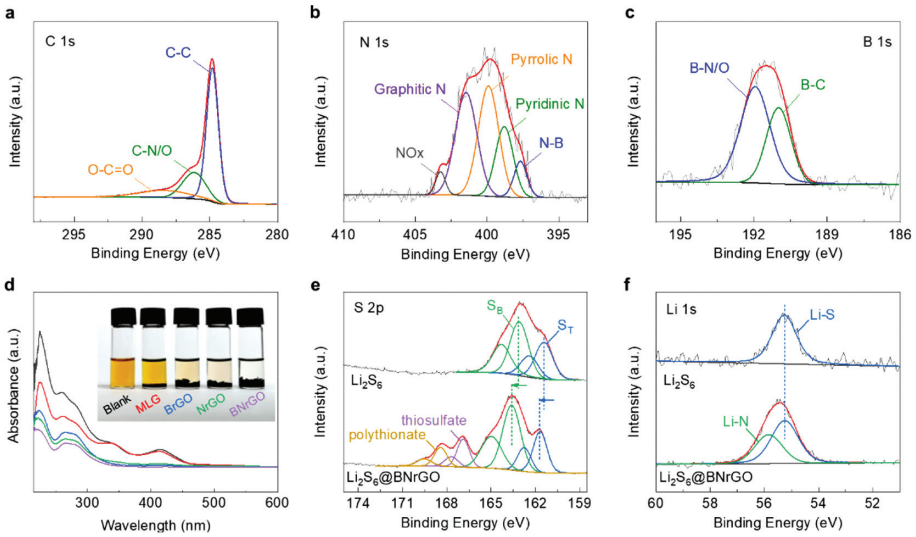

Fig. 3. XPS (a) C 1s, (b) N 1s and (c) B 1s spectra of BnrGO. (d) Optical photographs and the corresponding UV–vis spectra of LPS adsorption by different samples. XPS (e) S 2p and (f) Li 1s spectra of Li_2S_6 before and after adsorption by BNrGO.

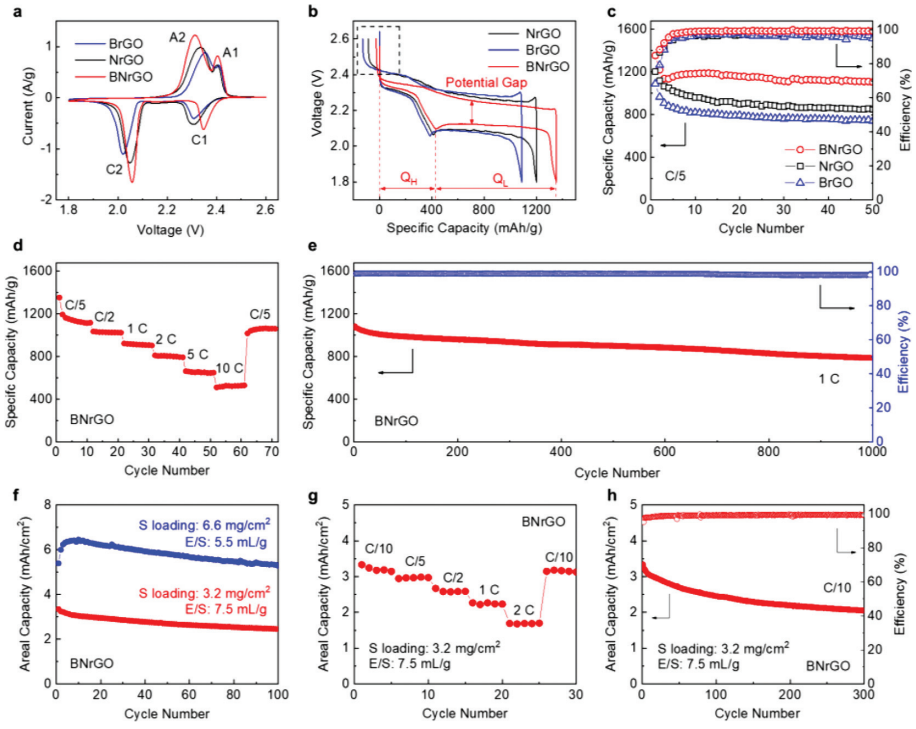

Fig. 4. (a) CV profiles, (b) charge-discharge curves, and (c) cycling performances at C/5 of BrGO, NrGO, and BNrGO cells. (d) Rate and (e) long-term cycling performance of BNrGO cells. (f) Cycling, (g) rate, and (h) long-term cycling performance of BNrGO cells at raised sulfur loading and limited electrolyte.

(1087.4 mAh/g) and NrGO (1200.4 mAh/g) cells. The Nyquist plots (Fig. S16 and Table S2 in Supporting information) reveal the smallest charge-transfer (43.42 *vs.* 35.7 and 77.18 Ω) of the BNrGO cell [38], which is responsible for its most facile and efficient sulfur reactions among these samples. Moreover, the BNrGO cell delivers the smallest overcharge rate (101.9%), which is defined as the quotient of the subsequent charge capacity divided by the initial discharge capacity (Fig. 4b and Fig. S17 in Supporting information), compared with NrGO (107.2%) and BrGO (111.9%). This signifies the effective shuttle inhibition enhanced redox reversibility by the co-doped design. For further verification, the self-discharge behaviors were further compared. The self-discharge profiles were recorded by cutting off the galvanostatic discharging at 2.25 V and rest for 12 h at the open-circuit voltage (OCV). As shown in Fig. S18 (Supporting information), the BNrGO cell shows the smallest voltage resilience at the cut-off point, implying its higher reduction efficiency than the other cells at the same operational voltage. Upon the OCV rest, very limited voltage and capacity losses (9.6 mV and 3.85%) are guaranteed by BNrGO, which is much less than those based on BrGO (16.9 mV and 8.42%) and NrGO (17.4 mV and 9.75%), strongly indicating the strong capability of BNrGO for constraining the shuttling behavior. Based on these results, the cycling performances of different cells are compared in Fig. 4c. The BNrGO cell retains 81.6% of its initial capacity after 50 cycles, which is

much higher than those of the BrGO (68.0%) and NrGO (70.6%) cells. Meanwhile, a consistently higher coulombic efficiency can be also obtained by BNrGO, certifying the excellent electrochemical reversibility. Further, the rate capability and long-term cyclability were explored as shown in Figs. 4d and e. The BNrGO cell achieves a considerable capacity of 526.6 mAh/g even at a high rate of up to 10 C. Besides, outstanding cycling stability over 1000 cycles can be also obtained at 1 C, demonstrating a minimum decaying rate of 0.027% per cycle with a constantly high coulombic efficiency close to unity. These performances are highly competitive among the recent literature (Table S3 in Supporting information), and further confirm the great superiority of the bidirectionally polarized BNrGO design.

To further explore the practical viability, the BNrGO cells with higher sulfur loading and lower E/S ratio were examined. As shown in Fig. 4g, the BNrGO cell with a sulfur loading of 3.2 mg/cm^2 and an E/S ratio of 7.5 mL/g retains a decently high areal capacity of 2.46 mAh/cm^2 after 100 cycles at 0.1 C. When further tightening the conditions to a sulfur loading of 6.6 mg/cm^2 and an E/S ratio of 5.5 mL/g, a high initial areal capacity of 6.46 mAh/cm^2 can be still accessible, which retains 5.32 mAh/cm^2 after 100 cycles. Such favorable sulfur utilization and redox efficiency should be attributed to the architectural and chemical designs of the BNrGO matrix, which provides fast electron/ion transfer and abundant active surfaces for reversible sulfur reactions. In addition, an areal capacity of 1.69 mAh/cm^2 is still attainable even at a high rate up to 2 C (Fig. 4h), further demonstrating the excellent reaction kinetics enabled by the BNrGO matrix. Given this, prolonged cycling was performed, which witnesses a stable cyclic behavior of the BNrGO cell with a constantly high coulombic efficiency and high capacity retention of 2.05 mAh/cm^2 after 300 cycles (Fig. 4f). It is noted that the obtained high-loading performance is superior to most of the recent literature based on the heteroatom-doped designs (Table S4 in Supporting information). This result further demonstrates the great capability of the bidirectional polarization strategy for approaching fast and durable sulfur electrochemistry, as well as its good potential in pursuing practically viable Li-S batteries.

In summary, we have demonstrated a bidirectional chemical polarization strategy for designing advanced host matrixes in Li-S batteries. The chemical superiority was firstly predicted by DFT calculations, and then experimentally verified by a series of physicochemical and electrochemical characterizations. The as-designed BNrGO combines electropositive B and electronegative N within the carbon lattice, which intensively heterogenizes the charge distribution and enables stronger chemical interactions with LPS over its mono-doped counterparts. As a result, superior sulfur immobilization and catalyzation were realized, contributing to excellent cycling stability over 1000 cycles and superb rate capability up to 10 C, as well as decent performance even under high loading and lean electrolyte. This work offers an instructive strategy for designing advanced host matrixes via doping engineering, holding a great promise in pursuing efficient sulfur electrochemistry as well as high-performance Li-S batteries.

Declaration of competing interest

The authors declare that they have no known competing financial interests or personal relationships that could have appeared to influence the work reported in this paper.

Acknowledgments

This work was financially supported by the National Natural Science Foundation of China (No. 22109072), the Natural Science Foundation of Jiangsu Province (No. BK20210349), the China Postdoctoral Science Foundation (No. 2021M691586), the Postdoctoral Research Funding Scheme of Jiangsu Province (No. 2021K446C), and the Shuangchuang (Mass Innovation and Entrepreneurship) Program of Jiangsu Province (No. JSSCBS20210208).

Supplementary materials

Supplementary material associated with this article can be found, in the online version, at doi:10.1016/j.cclet.2022.107811.

References

[1] P.G. Bruce, S.A. Freunberger, L.J. Hardwick, et al., Nat. Mater. 11 (2012) 19–29.
[2] B. Scrosati, J. Hassoun, Y.K. Sun, Energy Environ. Sci. 4 (2011) 3287–3295.
[3] A. Manthiram, Y.Z. Fu, S.H. Chung, et al., Chem. Rev. 114 (2014) 11751–11787.
[4] G.R. Li, S. Wang, Y.N. Zhang, et al., Adv. Mater. 30 (2018) 1705590.
[5] Y.X. Yin, S. Xin, Y.G. Guo, et al., Angew. Chem. Int. Ed. 52 (2013) 13186–13200.
[6] Z.W. Seh, Y.M. Sun, Q.F. Zhang, et al., Chem. Soc. Rev. 45 (2016) 5605–5634.
[7] S.L. Yu, W.L. Cai, L. Chen, et al., J. Energy Chem. 55 (2021) 533–548.
[8] L. Hencz, H. Chen, H.Y. Ling, et al., Nano-Micro Lett. 11 (2019) 17.
[9] Z.L. Xu, J.K. Kim, K. Kang, Nano Today 19 (2018) 84–107.
[10] Y.Z. Liu, G.R. Li, J. Fu, et al., Angew. Chem. Int. Ed. 56 (2017) 6176–6180.
[11] R.P. Fang, K. Chen, L.C. Yin, et al., Adv. Mater. 31 (2019) 1800863.
[12] L. Ji, X. Wang, Y. Jia, et al., Chin. Chem. Lett. 34 (2023) 107123.
[13] H.J. Peng, G. Zhang, X. Chen, et al., Angew. Chem. Int. Ed. 55 (2016) 12990–12995.
[14] Q. Pang, D. Kundu, M. Cuisinier, et al., Nat. Commun. 5 (2014) 4759.
[15] L.L. Zhang, Y.J. Wang, Z.Q. Niu, et al., Carbon 141 (2019) 400–416.
[16] J.P. Paraknowitsch, A. Thomas, Energy Environ. Sci. 6 (2013) 2839–2855.
[17] T.Z. Hou, X. Chen, H.J. Peng, et al., Small 12 (2016) 3283–3291.
[18] Y. Zhao, Z. Gu, W. Weng, et al., Chin. Chem. Lett. 34 (2023) 107232.
[19] Z. Ling, Z.Y. Wang, M.D. Zhang, et al., Adv. Funct. Mater. 26 (2016) 111–119.
[20] S.Y. Yuan, J.L. Bao, L.N. Wang, et al., Adv. Energy Mater. 6 (2016) 1501733.
[21] T. Schiros, D. Nordlund, L. Palova, et al., ACS Nano 10 (2016) 6574–6584.
[22] T.Z. Hou, W.T. Xu, X. Chen, et al., Angew. Chem. Int. Ed. 56 (2017) 8178–8182.
[23] M. Fang, X.Y. Liu, J.C. Ren, et al., NPJ Comput. Mater. 6 (2020) 8.
[24] J. Guerrero-Contreras, F. Caballero-Briones, Mater. Chem. Phys. 153 (2015) 209–220.
[25] G.R. Li, W. Lei, D. Luo, et al., Adv. Energy Mater. 8 (2018) 1702381.
[26] A.C. Ferrari, J.C. Meyer, V. Scardaci, et al., Phys. Rev. Lett. 97 (2006) 187401.
[27] Q. Pang, J.T. Tang, H. Huang, et al., Adv. Mater. 27 (2015) 6021–6028.
[28] K.L. Zhang, W.L. Cai, Y.F. Liu, et al., Chem. Eng. J. 427 (2022) 130897.
[29] Y. Zhao, L.J. Yang, S. Chen, et al., J. Am. Chem. Soc. 135 (2013) 1201–1204.
[30] Y.P. Xie, H.W. Cheng, W. Chai, et al., Chin. Chem. Lett. 28 (2017) 738–742.
[31] H.Q. Peng, X. Ming, K. Pang, et al., Nano Res 15 (2022) 4902–4908.
[32] H. Chen, C. Chen, Y.J. Liu, et al., Adv. Energy Mater. 7 (2017) 1700051.
[33] X. Liang, C. Hart, Q. Pang, et al., Nat. Commun. 6 (2015) 5682.
[34] G.R. Li, F. Lu, X.Y. Dou, et al., J. Am. Chem. Soc. 142 (2020) 3583–3592.
[35] W.L. Qiu, G.R. Li, D. Luo, et al., Adv. Sci. 8 (2021) 2003400.
[36] Y.Z. Wang, X.X. Huang, S.Q. Zhang, et al., Small Methods 2 (2018) 1700345.
[37] H.T. Qu, J.W. Ju, B.B. Chen, et al., J. Mater. Chem. A 6 (2018) 23720–23729.
[38] X.X. Gu, C.J. Tong, C. Lai, et al., J. Mater. Chem. A 3 (2015) 16670–16678.